

# Biomimetic FAA-certifiable, artificial muscle structures for commercial aircraft wings

Ronald M Barrett<sup>1</sup> and Cassandra M Barrett<sup>2</sup>

<sup>1</sup>University of Kansas Aerospace Engineering Department, USA

<sup>2</sup>College of Biological Sciences, University of Minnesota, Minneapolis, USA

E-mail: [adaptivebarrett@gmail.com](mailto:adaptivebarrett@gmail.com)

Received 1 February 2014, revised 24 March 2014

Accepted for publication 15 April 2014

Published 17 June 2014

## Abstract

This paper is centered on a new form of adaptive material which functions much in the same way as skeletal muscle tissue, is structurally modeled on plant actuator cells and capable of rapidly expanding or shrinking by as much as an order of magnitude in prescribed directions. Rapid changes of plant cell shape and sizes are often initiated via ion-transport driven fluid migration and resulting turgor pressure variation. Certain plant cellular structures like those in *Mimosa pudica* (sensitive plant), *Albizia julibrissin* (Mimosa tree), or *Dionaea muscipula* (Venus Flytrap) all exhibit actuation physiology which employs such turgor pressure manipulation. The paper begins with dynamic micrographs of a sectioned basal articulation joint from *A. julibrissin*. These figures show large cellular dimensional changes as the structure undergoes foliage articulation. By mimicking such structures in aircraft flight control mechanisms, extremely lightweight pneumatic control surface actuators can be designed. This paper shows several fundamental layouts of such surfaces with actuator elements made exclusively from FAA-certifiable materials, summarizes their structural mechanics and shows actuator power and energy densities that are higher than nearly all classes of conventional adaptive materials available today. A sample flap structure is shown to possess the ability to change its shape and structural stiffness as its cell pressures are manipulated, which in turn changes the surface lift-curve slope when exposed to airflows. Because the structural stiffness can be altered, it is also shown that the commanded section lift-curve slope can be similarly controlled between 1.2 and 6.2 rad<sup>-1</sup>. Several aircraft weight reduction principles are also shown to come into play as the need to concentrate loads to pass through point actuators is eliminated. The paper concludes with a summary of interrelated performance and airframe-level improvements including enhanced gust rejection, load alleviation, ride quality, fatigue life and flight safety.

Keywords: adaptive, FAA certifiable, active, pressure, honeycomb, pneumatic, hydraulic

## Nomenclature

		$C_L$	aircraft lift coefficient	~	
		$C_{L\alpha}$	aircraft lift coefficient WRT	$\alpha$ rad <sup>-1</sup>	
		$C_{L\delta f}$	aircraft lift coefficient WRT	$\delta_f$ rad <sup>-1</sup>	
$c_h$	effective hinge moment coefficient	~	$E_m$	mass specific energy density	J kg <sup>-1</sup>
$c_{h\alpha}$	effective hinge moment coefficient WRT	$\alpha$ rad <sup>-1</sup>	$E_p$	peak shot voltage	kV
$c_{h\delta}$	effective hinge moment coefficient WRT	$\alpha$ rad <sup>-1</sup>	$E_v$	volume specific energy density	J m <sup>-3</sup>
$\bar{C}_f$	mean geometric chord of PAH flap	m	$I_p$	peak strike current	A
$C_l$	section lift coefficient	~	$K_\delta$	PAH flap effective stiffness	N m rad <sup>-1</sup>
			$L$	total aircraft lift	N
			$L_{\text{command}}$	commanded total aircraft lift	N

$M_\delta$	PAH flap root moment	N-m
$P$	peak strike electrical power	W
$\bar{q}$	dynamic pressure	Pa
$S$	wing area	m <sup>2</sup>
$S_h$	PAH flap surface area	m <sup>2</sup>
$\alpha$	angle of attack	°
$\delta_{\text{command}}$	PAH flap commanded deflection angle	°
$\delta_f$	PAH flap effective deflection angle	°
$\epsilon$	strain	~
$\eta$	transfer efficiency	~
$\sigma$	stress	MPa

### Acronyms

BCDP	balanced cell differential pressure
CDP	cell differential pressure
PAH	pressure adaptive honeycomb
UAV	uninhabited aerial vehicle
UCDP	unbalanced cell differential pressure

## 1. Introduction and motivation

For more than a century, researchers have actively examined a wide variety of adaptive or ‘smart’ materials for aerospace applications. Although much research has been conducted on a variety of sensing, communications and control applications, only a handful have been integrated into secondary aircraft structures on FAR-23/25 certified aircraft. Crawley and his team at MIT were among the first to integrate adaptive actuators into low aspect ratio plates and aerodynamic surfaces [1]. These innovations were rapidly followed by integration of adaptive materials in missile fins, missile wings and uninhabited aerial vehicle (UAV) components [2–4]. The first ‘Adaptive Aerostructures’ patent was first filed in 1989, issued in 1995, and was centered on a technique which would allow adaptive materials of many classes to be used as highly directional actuators, working like muscle tissues to manipulate rotor blades, missile wings and fins [5]. This first adaptive aerostructures patent employed a biological analog to induce shear flows along the lengths of lifting surfaces and supporting structures. Figure 1 shows the basic kinematic anatomy of a twisting human forearm with diagonally configured pronator and supinator muscle groups inducing moments about the radius and ulna skeletal structure.

This diagonal placement of muscles was mimicked in some of the first aerodynamic structures to use adaptive materials to twist lifting surfaces. Figure 2 shows diagonally placed directionally attached piezoelectric (DAP) elements under the skin of a missile wing which induced shear torsional flows to twist the wing about the main and rear spars. By observing the active kinematics of the arrangement, it can be seen that the spars function much in the same way as the radius-ulna pair in the human forearm while the DAP

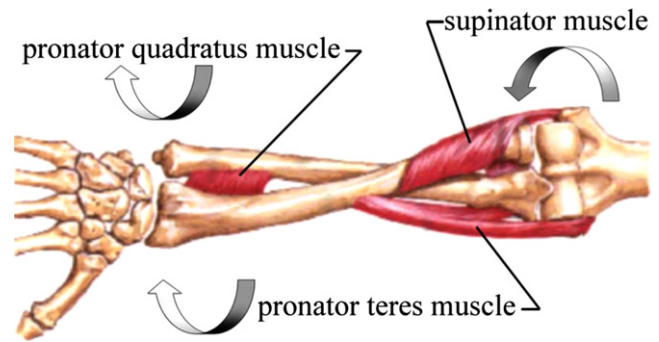


**Figure 1.** Human forearm with twist activation via pronator and supinator muscle groups.

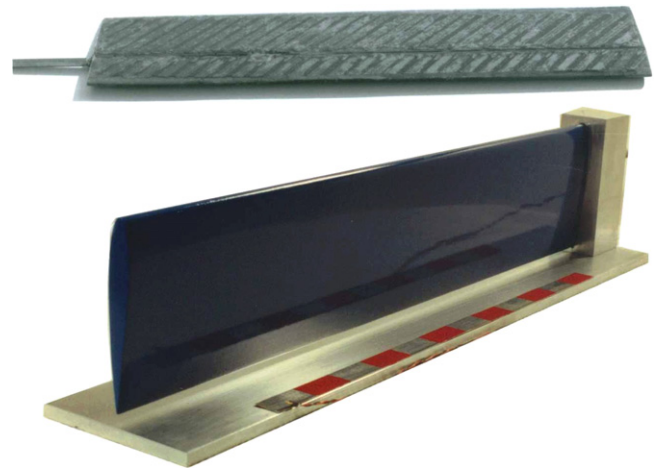


**Figure 2.** Twist-active missile wing prior to skinning showing shear-flow inducing DAP elements and after skinning.

elements actively twist the wing in the same way that the supinator–pronator muscle groups turn the wrist relative to the elbow.

In so many ways, many of the earliest adaptive aerostructures also had clear biological analogs. Helicopter rotor blades using DAP elements exhibited the same fundamental structure as above. The first UAVs to employ adaptive materials for all flight control took to the air 20 years ago and used a segmented approach to actuation in their MicroFlex stabilators like phalanges undergoing manipulation by extensor–flexor muscle pairs. More analogs followed in numerous hard-launched bullet and cannon shell actuators efforts. These schemes employed arrangements like the bicep–tricep muscle pair which rotates the forearm about the elbow joint to rotate a balanced supersonic nose about a body-mounted hinge [6].

A large body of work on rotorcraft actuators which had biological analogs with first flight in September 1997 using DAP elements to pitch Hiller servopaddles in a forearm supinator–pronator arrangement [7]. Straub and his team employed a variety of leveraging schemes to amplify motions of rotor blade flight control and vibration suppression actuators. These actuators used mechanisms bore some similarities



**Figure 3.** FAA-certified Brittain Industries BI707. Rudder boost pneumatic servo assembly (12" scale).

to the bicep–tricep motion amplification scheme used to pivot the forearm about the elbow [8–11].

Some of the most important biomimetic flight control actuator arrangements which were conceived and reduced to practice exhibited extremely low power consumption with vastly improved deflection levels. Lesieutre and his team developed methods of achieving electrical-to-mechanical conversion efficiencies of nearly 100% with adaptive materials by employing reverse-bias mechanisms in low-net passive stiffness (LNPS) structures [12, 13]. These LNPS structures were expanded and integrated into a number of aircraft structures through the 2000s [14–17]. Although they functioned well and were used in a number of flight test and are found in serial production aircraft, they relied upon materials which were (and are) fundamentally not FAA-certifiable for use in primary structure.

Although nearly all classes of adaptive aerostructures suffer from this property of being fundamentally uncertifiable because of a lack of a certifiable materials database, one family of flight control actuators skirts this problem by drawing upon historical FAA certified flight control technology. For more than a half-century, the FAA has certified a series of highly reliable, fast, lightweight flight control actuators which are based on pneumatics. The flight service record of these actuators stretches from the Beech Bonanza of the 1940s to the King Air series aircraft in production today. Figure 3 shows a basic layout of this concentrated point, push–pull actuator which is capable of 92% contracted length extension with under 0.6% energy loss per stroke [18, 19]. This class of King Air pneumatic rudder actuator weighs under 1.5lb (0.68 kg) and yet can generate in excess of 100lb (445 N) of force which remains constant over the entire stroke length.

A number of adaptive structures technologists have also explored other configurations of pneumatic point actuators. Wereley and his team investigated several pull–pull actuator configurations using filament-wound pneumatic bladders which are capable of shrinking in length upon application of high internal pressure levels. These actuators were shown to

be capable of high force levels and were demonstrated to hundreds of thousands of cycles for use in both fixed-wing aircraft and rotorcraft [20, 21].

Although current pneumatic actuators clearly function well, as they have been flying in FAA certified aircraft for 60 years, such point actuators demand the integration of hinges, linkages, tracks and/or other comparatively heavy hard points in aircraft structures. In 2007, a new approach to adaptive wing structures using strictly FAA-certifiable materials, pneumatics and bio-inspired configurations was conceived and reduced to practice [22–24]. These pressure adaptive honeycombs (PAH) were designed around conventional, certified aerospace materials like 2024-T0 aluminum, AISI-305 stainless steel and Kevlar™-epoxy aramid. Figure 4 shows the first PAH trailing edge specimen undergoing camber deformations in a vacuum chamber, simulating aircraft altitude variations [22].

If one examines the overall performance of PAH with respect to other classes of adaptive materials using either atmospheric pressure variations or forced internal cell pressure changes, then the blocked stress and maximum strains can be plotted as seen in figure 5 [23].

Clearly in terms of total volumetric energy density, high pressure PAH possesses superior properties with respect to most other classes of adaptive materials. What is more is that it is strictly made from certifiable materials, which should ease the path towards certification. While PAH is certainly a viable option in terms of actuator configuration, many lessons can be learned from mother nature with respect to bidirectional actuation. The coming sections present the physiology of bidirectional anatomical structures based on cellular actuators which function in ways similar to PAH and structural arrangements which follow.

If one examines a different metric than  $J m^{-3}$  as was put forth in figure 5, then a more meaningful measure of the applicability for aerospace actuators can be seen. Figure 6 shows not how many Joules of work are available per unit volume, but per unit mass. Because aircraft are often more weight critical than volume critical in actuator components.

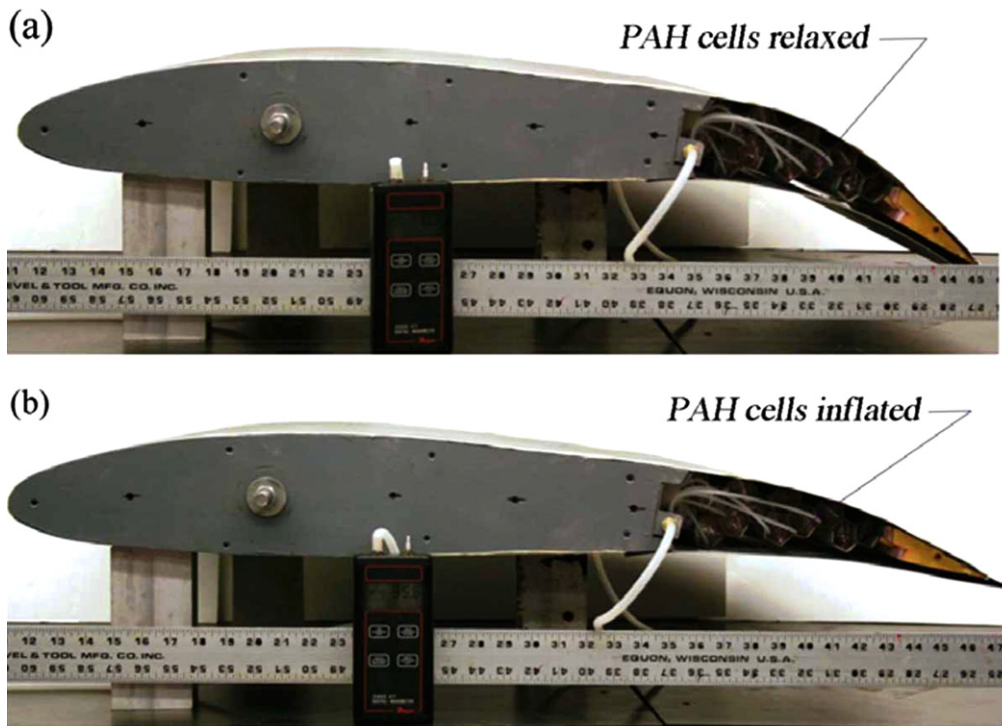


Figure 4. Pressure adaptive honeycomb flap section in vacuum chamber [22].

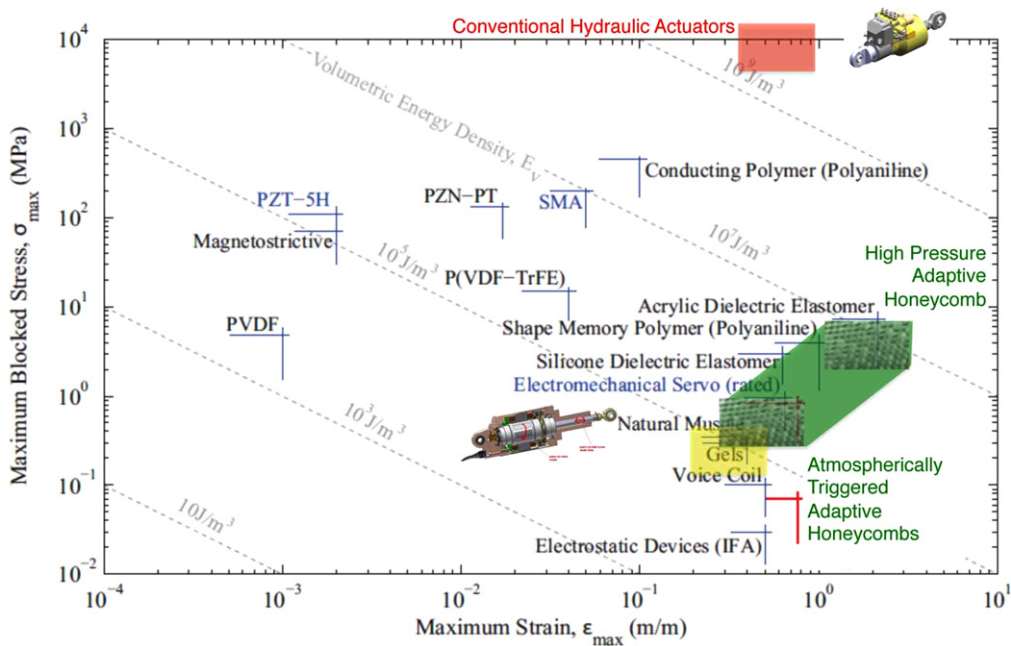


Figure 5. Blocked stress versus max. strain for major actuator classes [23].

Another weight saving effect will be in the very way that aircraft structures are built. The current overall structural design philosophy of aircraft flight control structures is to (i) absorb distributed loads, (ii) concentrate distributed loads to finite hard points, (iii) run hard point loads through finite actuators, tracks and brackets, (iv) terminate actuator, track and bracket loads at another location, (v) redistribute loads. This

progression is shown in figure 7. To fully take advantage of the favorable properties of PAH, it is necessary to leave distributed loads distributed then pass them through distributed actuator and control mechanisms. Clearly weight decrements would be incurred by elimination of hard point connections, tracks, brackets and hinges, and there would be a net wetted area saving in that the flap track fairings would be eliminated.

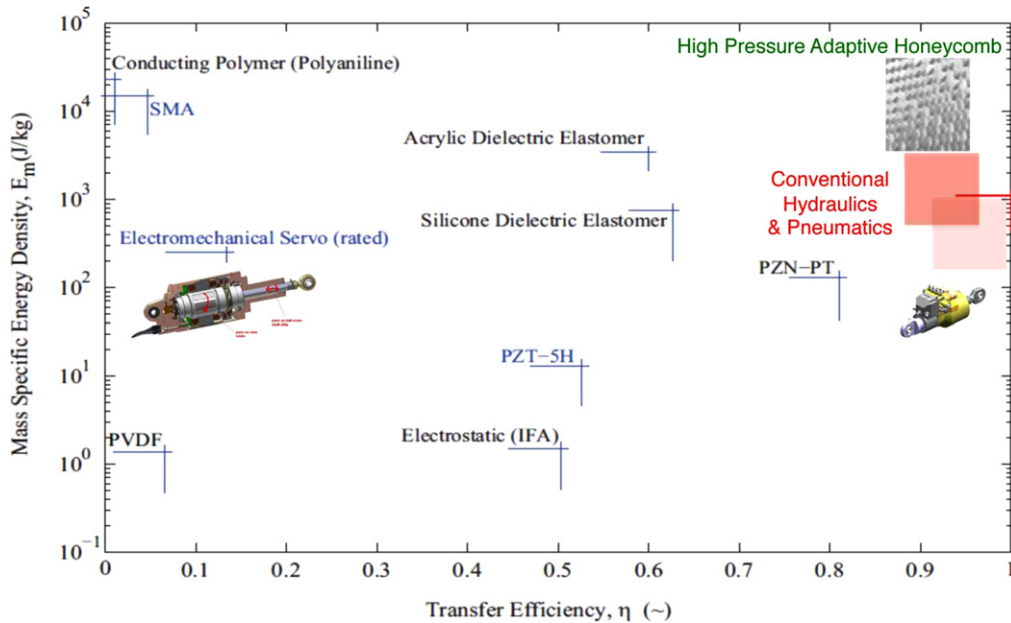


Figure 6. Actuator mass specific energy density and transfer efficiency [23].

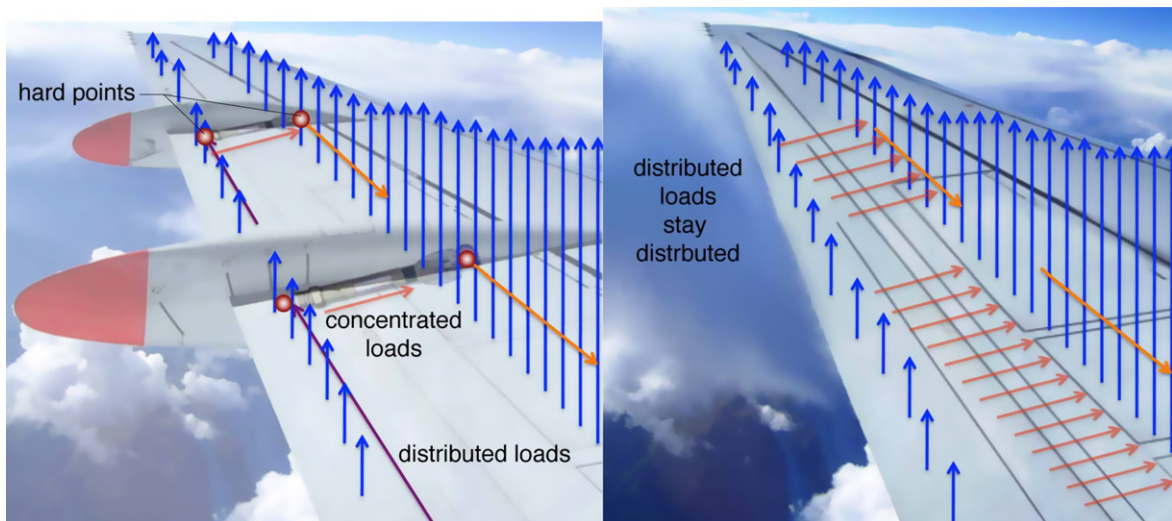


Figure 7. Overall difference between conventional and PAH secondary flight control concepts.

## 2. Short time scale actuators in nature

In an effort to increase the utility of the existing PAH actuators, several different classes of natural actuators are examined. Plant models in particular are explored as suitable analogs.

### 2.1. A review of short time scale actuators in biology

The biological world presents a myriad of short time scale actuation mechanisms of potential interest as analogues to adaptive structures. One of the most ancient of these is the flagellar movement of many microorganisms such as *Escherichia coli* and certain protists such as dinoflagellites. The flagellar protrusion attached to the cell by the basal body propels the cell with whipping or whirling motions and is

conserved in mammalian cells such as spermatozoa. Pili and cilia are more numerous yet propel the cell similarly. Some protists use cytoplasmic extensions known as pseudopodia to attach to nearby surfaces in order to propel the cell forward. These systems serve as well studied models of microbial motion, although certainly a great diversity exists. Parasitic actin rearrangement such as that utilized by *Listeria monocytogenes*, excretion propulsion, and coordinated cellular rearrangements of slime molds show the diversity of microbial motion; however a multicellular model will better serve the purposes of this paper, illustrating motion in adaptive materials [25].

As cells assemble into more complex, multicellular systems we see synchronized cellular coordination, which is key to our purposes here in exploring dynamic, cell-based materials such as PAHs. Most readers will have some basic



**Figure 8.** Mimosa frond open, partially closed, closed (photo credit: C Barrett).

familiarity with the workings of animal muscle tissues, which involves contraction of cellular tissues via actin rearrangement within individual cells of a muscle group. A closer look at the mechanism reveals a complex series of chemical reactions including the hydrolysis of ATP that induce conformational changes in myosin fibers and the activation of troponin for binding by calcium ions. Together the fibers bind actin within the cell to induce large scale, coordinated conformational changes that induce muscle contraction [26]. This mechanism is conserved throughout the animal kingdom in various forms. Although the overall scheme for animal muscle fiber stimulation and contraction is not easily replicated in mechanical systems with certifiable materials, it can easily be shown that this challenge is not seen with some plant articulation mechanisms.

## 2.2. Short time scale actuators in the plants

Short time scale actuators that induce large scale motion in plants are comparatively rare. *Mimosa pudica* (sensitive plant), *Albizia julibrissin* (Mimosa tree), and *Dionaea muscipula* (Venus Flytrap) are a few of the most well studied examples and all employ a remarkably similar mechanism to induce short time scale macroscopic conformational changes. The essence of the actuator is a swift drop in turgor pressure at the pulvinar joint due to a change ion gradation that pulls water from the cell. Water is released from internal vacuoles to bring the cell to a plasmolyzed state. Within the cytoskeleton actin fiber rearrangement stabilizes internal structures during changes in turgor pressure via fragmentation. The

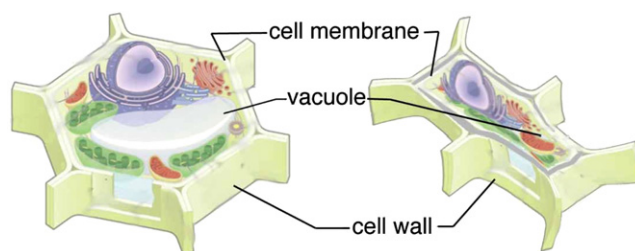


**Figure 9.** Hypertonic and hypotonic articulation cellular configurations.

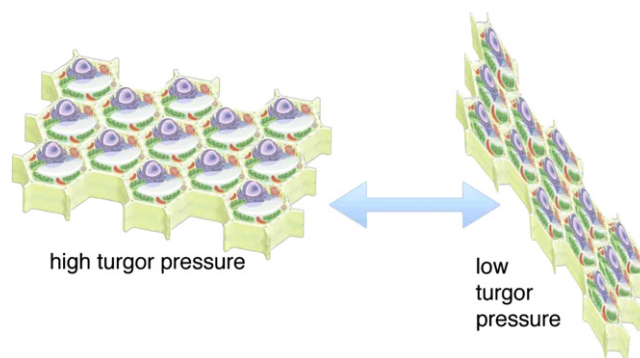


**Figure 10.** Lateral contraction, extension and shear of plant cell tissues with variation in hydration.

swift collapse of cells at the joint causes the structures above to fall inwards to a closed state. Figure 8 shows the macroscopic consequences of this mechanism in *A. julibrissin*. The photos show a timelapse sequence of a mimosa tree frond as it closes, most likely due to stress. Closure is attained swiftly and completely from the open state [27–29].

The cells at the pulvinus or joint at the base of each individual leaf undergo drastic reconfirmation within a short time period. Ionic signals are sent as a response to several possible stimuli including heat, touch (especially in the case of the Venus fly trap), and light. Likewise these signals can be hormonal and part of the plant's daily life cycle. In either case, the influx of ions, typically potassium, induces a hypertonic state around the cell, inducing the release of water from the cell to regulate surrounding ion concentrations. The gradient change leads to a swift release of water stored in internal vacuoles. Actin within the cytoskeleton fragments as the cell bends and the hypotonic cell state in figure 9 is attained [27–29].

This rapid collapse of flexor cells at the base of the leaf induces the characteristic closure of the joint. Of course collapse must be coordinated by groups of flexor cells. Figure 10 shows the effects of swift turgor pressure drop on a group of cells, making the resulting angled bending effect more obvious.

Figure 11 puts to scale the pulvinus in an open state in which cells remain turgid. Pressure from parenchymatous flexor cells at the joint, shown in the micrograph below in purple, stabilizes the structure to maintain its open state. The reentry of water via osmosis is also what allows the cell to return from a closed to an open state. It should be noted that

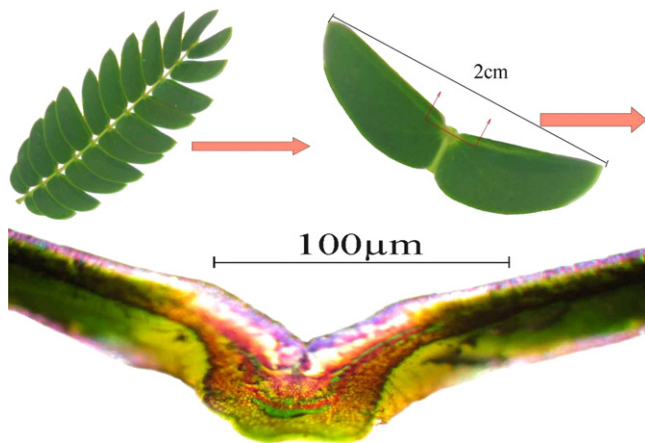


**Figure 11.** Section orientation of section across the pulvinus (photo credit: C Barrett).

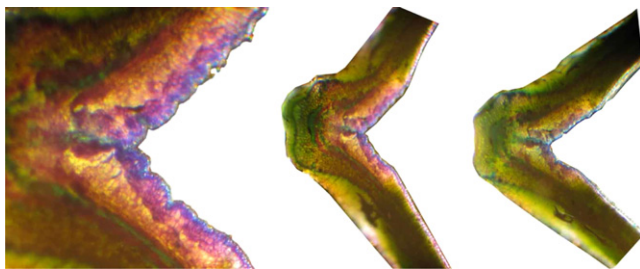


**Figure 12.** Pulvinus closeup and during actuation from  $110^\circ$  to  $70^\circ$  of aperiens (photo credit: C Barrett).

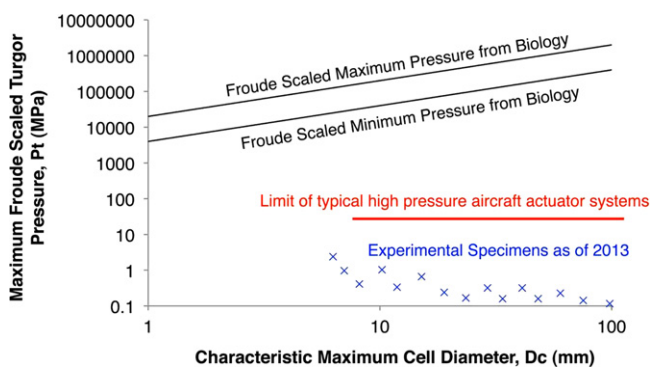


**Figure 13.** Effect of cell size, Froude-scaled pressure, limits and experimental specimens as of 2013.

the parenchymatous joint cells in the open state are relatively compact and inflated, creating a smooth outer surface [27, 28].

With stimulus the joint begins to change shape drastically. The joint cells deflate and are loosely arranged, allowing water to flow out to the intracellular space. Figure 12 shows a close up of articulation as the joint cells collapse after stimulus. This articulation of the parenchyma is facilitated by the aforementioned actin fiber fragmentation that occurs during closure [29]. This elegant mechanism of short time

scale actuation forgoes much of the complexity attributed to animal muscle tissues making it a suitable model for certifiable adaptive materials. Both closed and open states are easily and quickly reversible, while still inducing drastic conformational change on a larger scale (figure 13).

### 3. Biomimetic engineering solution to certifiable artificial muscles: pressure adaptive honeycomb (PAH)

A number of investigators have examined the benefits of using PAH type structures. [30, 31] show how PAH can be tailored to cantilevered structures and for reshaping of the nose of airfoils. If one examines the structures of [30, 31] and the micrographs of figures 9 and 10, it can be seen that several scaling laws and principles can help guide the orders of magnitude for actuation on larger structures. Given that figures 9 and 10 show pulvinar cells ranging from 200–1000 nm in major dimension and [31] reports turgor pressures from 400 kPa to 2 MPa. By using a number of scaling laws including Froude and Cauchy relations, it is easy to see that if one increases the cell size, then the scaled operating pressure would go up. By examining figure 5, it is obvious that the higher the operational pressures, the greater the amount of work per unit volume can be achieved. Plotting this pressure scaling trend against characteristic maximum cell diameter reveals why nature has evolved such small cells, as is made clear in figure 11. It is also interesting to note that the outer membranes of the largest cells found in nature, those of avian ova, are made from some of the stiffest materials in the natural world. Unlike smaller cells, stiff cell walls are necessary as size increases to maintain structural stability and flexural stiffness as the effective structural integrity available from BCDP is simply not able to keep pace with scaling laws. In man-made adaptive honeycombs, high strength cell walls can be made from aramids, or high strength isotropic metal foils like stainless steel.

From figure 11 it is obvious that the current state of the art in the PAH cells as of 2013 is many orders of magnitude off where scaled cells would reside. If one examines an upper practical bound representing current conventional hydraulic actuator technology, one can see that PAH is operating one to two orders of magnitude below current hydraulic actuator limits. This, of course indicates that there is substantial room for improvement. The reader will also note that there is a general trend for higher cellular operating pressures with reduced size of the PAH element. This typically comes as a limitation of current materials. Similarly, the lower bound on such man-made cells is currently below 10 mm using high strength structural materials. Accordingly, the forefront of PAH research is to balance manufacturing cost, performance and actuator energy density to arrive at an optimal actuator configuration for a given application.

Figure 11 clearly shows that structures with extremely small cells (those found in the natural world) operate at extremely high pressures while the specimens which use man-made cells can only function at much lower pressure levels.

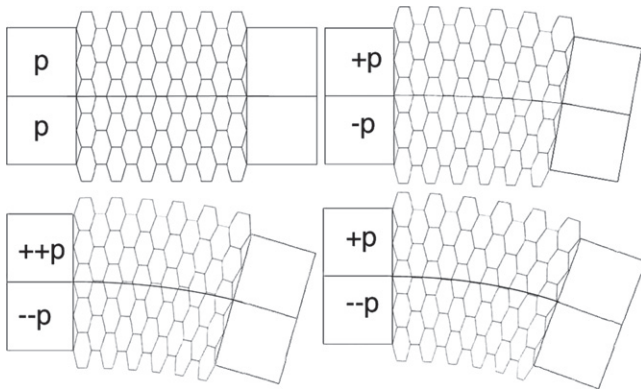


**Figure 14.** Bidirectional actuation scheme of PAH flight control actuator illustrating the effects of BCDP and UCDP manipulation.

This represents a profound balance as with high cell counts consistent with small cell sizes, manufacturing costs go up. However, operating pressures also go up which increases actuation energy and power densities. Conversely, minimization of manufacturing costs tends to drive cell counts down and cell sizes up. Ultimately, it is most likely that a given market will speak to the balance between cell size and acquisition costs to arrive at a system optimum.

## 4. PAH wing section performance

### 4.1. Structural modeling

To demonstrate the utility of the PAH system beyond what has been shown in [22–24], a subscale demonstrator was built by using a bidirectional actuator core. Figure 14 shows the fundamental arrangement of the honeycomb core during actuation with the PAH being arranged symmetrically on either side of a flexible substrate, bounded by end blocks. As the cell differential pressure (CDP) is manipulated, the PAH curves up or down in an effort to reach equilibrium. Figure 14 shows a downward stroke in response to working fluid addition to the upper cells and resulting compression and/or fluid extraction in the lower cells. At this point, it should be noted that two different forms of CDP are both manipulated and arise from testing and operational conditions. The balanced cell differential pressure (BCDP) of a bimorph PAH actuator layout is that gage pressure with respect to the outside static environment which is present such that when unloaded, the actuator will take the prescribed jugged or manufactured shape. The unbalanced cell differential pressure (UCDP) is the difference in CDP between the upper and lower PAH cells. The reader should note that a multitude or gradient of UCDPs are perfectly possible to achieve in a given structure depending on how it is being both loaded and controlled.

If one calls upon the modeling techniques of [22–24], it is easy to see that BCDP dominates the stiffness of a properly designed PAH actuator element. At a given deflection level, if one assumes a balanced BCDP during actuation, but closed actuator valves, then a fixed mass estimate is the appropriate

model. Figure 15 shows the stiffness-strain relations in the  $x$  and  $y$  directions for such a structure from [22]. From figure 15 it is easy to see that the closed cell (constant mass) model leads to a comparatively stiff structural element, with global stiffness increasing as the BCDP increases. It can similarly be observed that even though a structure may be balanced with equal BCDP on either side of a substrate, a stiff structural member is easily achieved simply by increasing BCDP. Also, reducing the BCDP will eventually lead to an extremely compliant structural member, bearing only the passive stiffness of the element itself.

It should also be noted that the longitudinal and lateral stiffness of the PAH when the cells are in the vicinity of a regular hexagon shape is minimized. This, however, is the typical neutral jugged position which results in maximum stroke and force generation capability from a manufacturing point of view.

### 4.2. Experimental setup

To demonstrate the utility of the PAH concept beyond what has been shown in [22–24], a 15 cm span, 15 cm chord NACA 0012 airfoil section was manufactured and wind tunnel tested. Figure 16 shows this wind tunnel model which was fabricated with a 3 mil ( $76\ \mu\text{m}$ ) thick AISI 1100-0 aluminum foil skin and fitted with a 300 grit roughness trip strip at the 10% chord.

The airfoil test section was constructed with a 2 lb/cuft polystyrene foam core section forming the first 70% of the internal structure. The PAH actuator and trailing-edge former both occupied the last 15% of the chord each as shown in figure 17.

The auxetic cell PAH actuator was molded from Kevlar 29 sheets of 0.05" ( $127\ \mu\text{m}$ ) thickness with 0.001" ( $25\ \mu\text{m}$ ) wall internal bladders constructed from. All six cells were ganged together via common, shared pressure ports. Figure 18 shows the geometry of the auxetic cellular structure of the actuator. The reader will note that the cell structures in figure 12 at the internal edges of the pulvinus exhibit strong corrugation. At the lower limit of macroscopic fabrication techniques using materials like aramid-epoxies, a structural approximation is to fold the structure into an auxetic cellular structure. Figure 18 shows how these accordian-like folds are arranged into two counteracting moment-generating rows of actuator cells. The six upper cells were designed to operate with the same internal pressures. Similarly, the six lower cells operate with the same internal pressures (which are often different than those on the other side). All structures in the Auxetic actuator were built from 5 mil ( $127\ \mu\text{m}$ ) thick Kevlar-29-epoxy cloth composite materials on a 5 mil ( $127\ \mu\text{m}$ ) substrate in the center of the actuator. It should be noted that the apexes of the actuator were rendered flexible by the thermal removal of the Pro-Set Lam-125/Lam-224 epoxy at approximately 580 °F (304 °C) applied in 4 mil ( $102\ \mu\text{m}$ ) wide strips.

The Kevlar 29 auxetic actuator was bonded to the rear of the forward polystyrene foam former with Hysol 9412 adhesive as was the trailing edge of the actuator to the aft

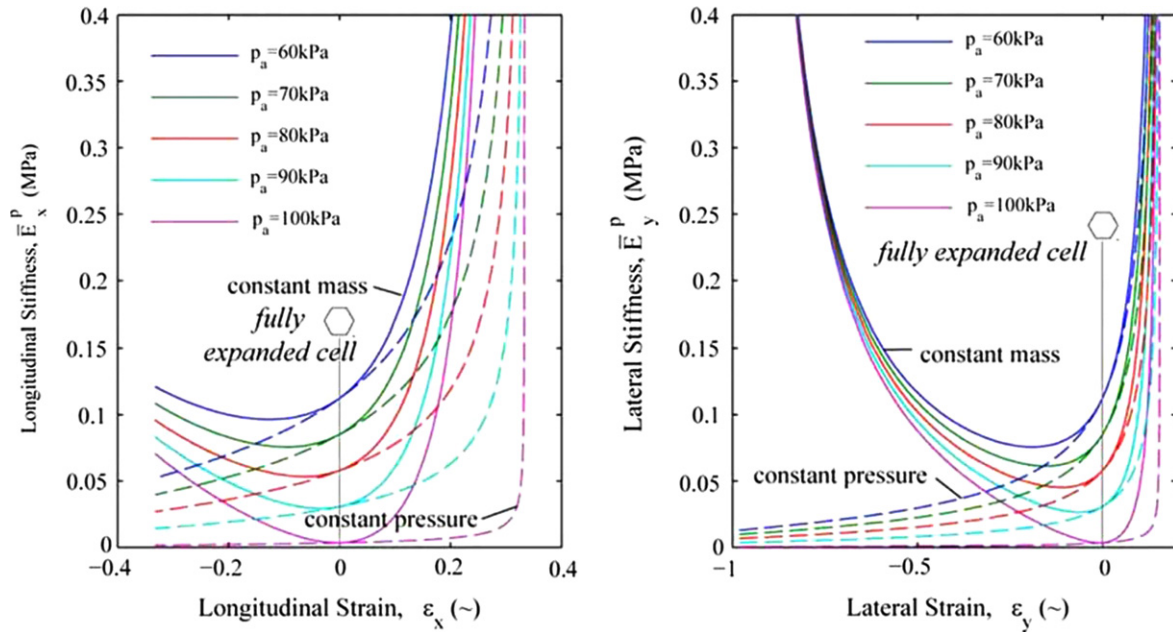


Figure 15. Stiffness–strain relations for low passive stiffness PAH considering varying levels of BCDP [22].

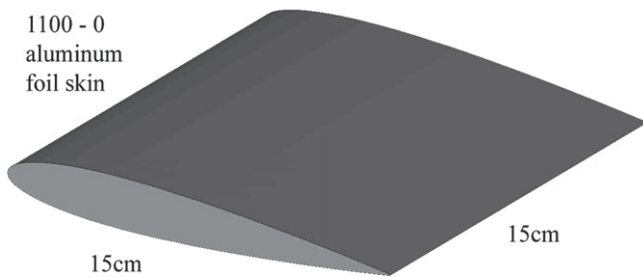


Figure 16. 15 cm NACA 0012 PAH wind tunnel test model.

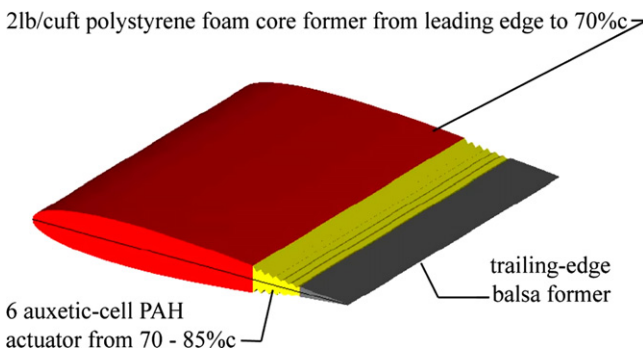


Figure 17. Internal polystyrene foam core formers and 6-auxetic cell PAH actuator.

foam core former. Figure 19 shows the free actuator with 1/8" (3 mm) silicone OD supply lines attached to the auxetic Kevlar actuator along with an aluminum-covered trailing-edge former.

Figure 20 shows the assembled airfoil section prior to mounting in the wind tunnel, including the actuator prior to and after installation of the 3 mil (76 μm) thick 1100-0 aluminum actuator cover.

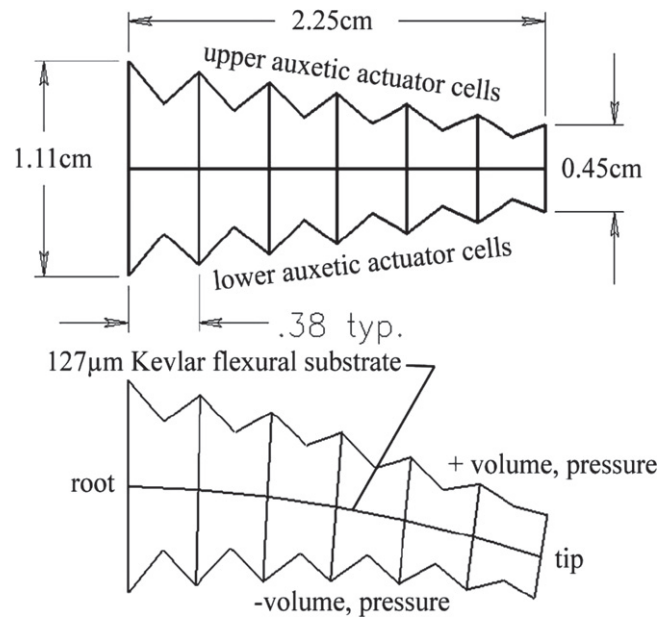


Figure 18. Cross-section of the Kevlar 29 auxetic actuator core geometry (dimensions in cm).

#### 4.3. Bench test results

The airfoil was tested for both maximum deflection and blocked trailing edge force as a function of unbalanced cell differential pressure (UCDP). Trailing edge deflection angles were measured at a maximum of up to 32°. (unloaded). These were initially observed at UCDP as low as 5 kPa. The airfoil was clamped in a rigid jiggling fixture and exposed to a variety of UCDPs with the trailing edge blocked. Figure 21 shows the results from bench testing. Deflections were measured using non-contact laser reflection techniques, accurate to ±0.05°.

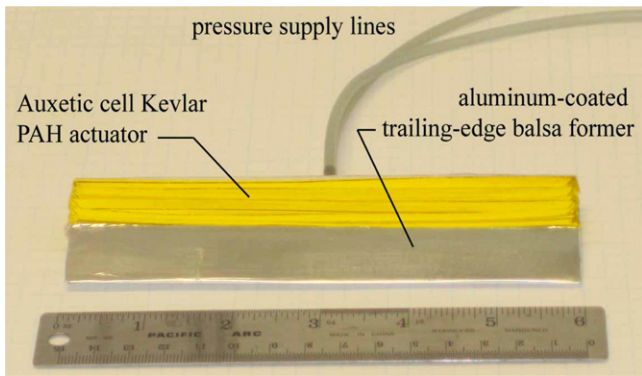


Figure 19. 15 cm NACA 0012 PAH wind tunnel test model.

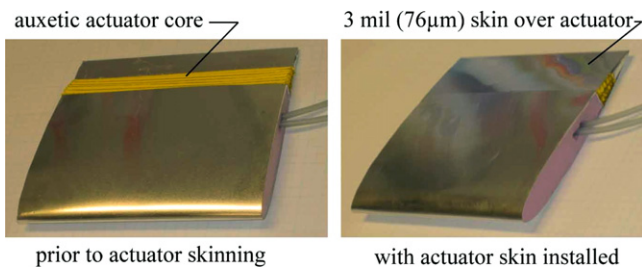


Figure 20. 15 cm square NACA 0012 test section without and with aft actuator skin mounted.

4.4. Wind tunnel testing

For this study, the specimen was run open loop with all valves closed and the airfoil set to a null position. The trailing edge was free to deform and deflect with angle of attack. Figure 21 shows the averaged first-cycle lift-curves with angle of attack at  $30\text{ m s}^{-1}$ ,  $100.6\text{ kPa}$  of atmospheric pressure, 63% relative humidity. All wind tunnel test data was corrected using the procedures of Barlow, Rae and Pope [32].

The airfoil was fitted between a pair of boundary layer splitter plates and operated at BCDPs of up to  $100\text{ kPa}$ . The airfoil section of figure 16 was tested in the University of Kansas Low Speed wind tunnel at speeds up to  $30\text{ m s}^{-1}$ . Data were taken via a four element force balance measuring lift and pitching moment through angles of attack ranging from  $-12$  to  $+12^\circ$ . Data was acquired by a 16 channel National Instruments NI USB-6259 data acquisition system, sampling at  $1\text{ kHz}$  per channel. Figure 22 shows the model mounted in the tunnel between splitter plates at  $3^\circ$  angle of attack with flat and trailing-edge commanded to deflect to approximately  $10^\circ$ .

Testing was conducted through a variety of BCDPs to demonstrate that the aerodynamic stiffness of the airfoil can be manipulated. It should be noted that mounted just  $1\text{ cm}$  away from the boundary splitter plate, a cross-feed valve can be opened or closed for upper or lower PAH cells. For the following series of tests, the actuators were pressurized to a given level with a flat trailing edge, then the valve was closed. This means that from instant to instant the unbalanced CDP can go higher than the prescribed amount of pressure as the mass contained within each actuator is approximately the

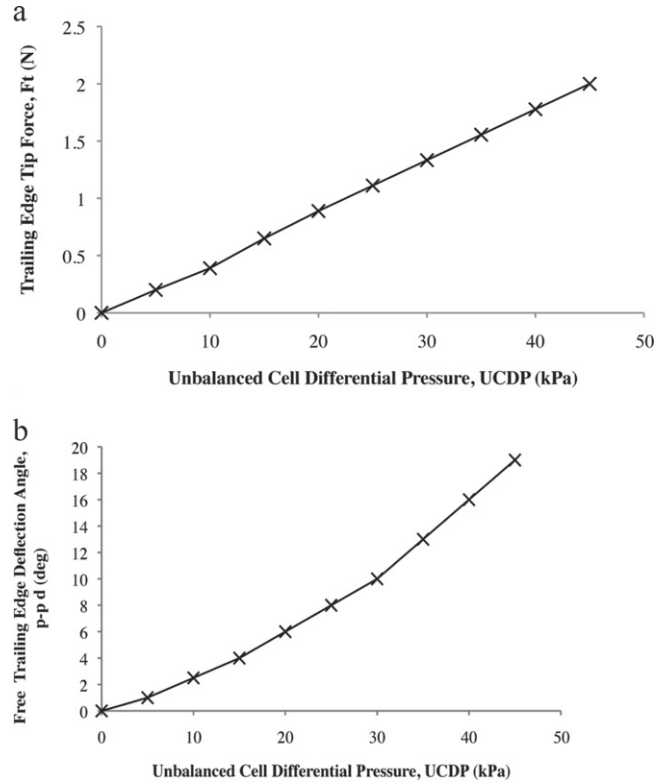


Figure 21. (a), (b) Trailing edge blocked force and trailing edge tip deflection levels with UCDP.

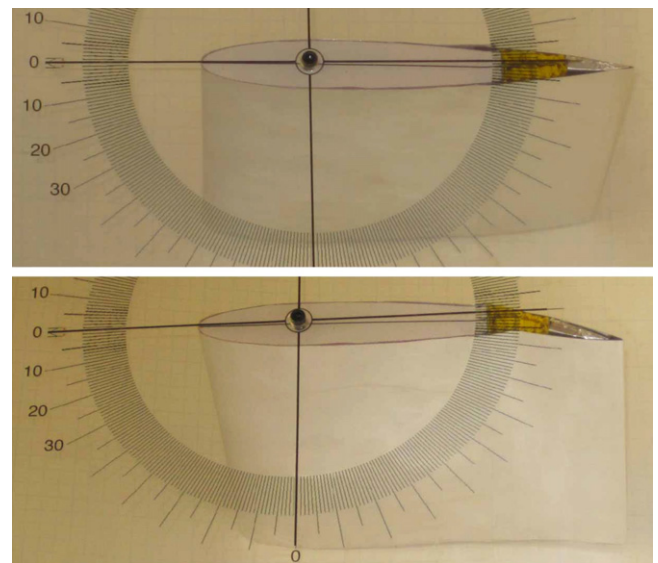
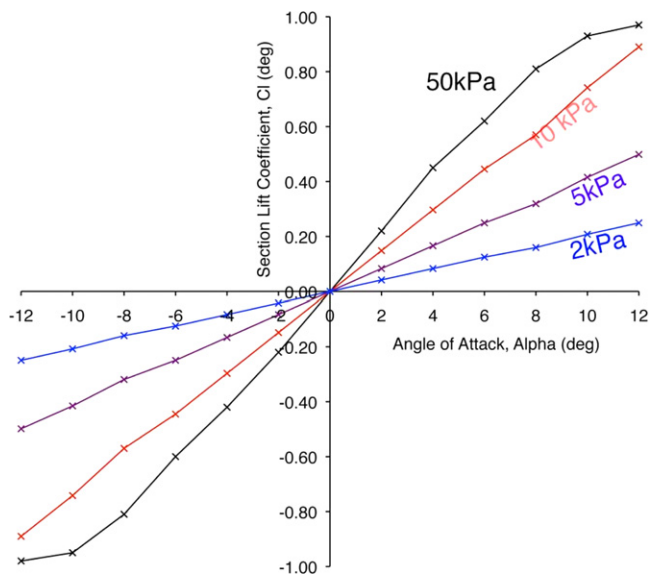


Figure 22. 15 cm NACA 0012 airfoil section mounted in the University of Kansas  $21 \times 30''$  ( $53 \times 76\text{ cm}$ ) subsonic wind tunnel with flat and  $10^\circ$ . Trailing-edge deflection command at  $10\text{ m s}^{-1}$ .

same. Figure 23 shows that the airfoil stiffens substantially with higher BCDP levels and closed cross-feed valve setting.

Clearly from figure 23 it is obvious that at  $50\text{ kPa}$ , the BCDP is so great that the total deformations of the trailing edge are negligible and the airfoil behaves as if it is solid at this dynamic pressure. As the BCDP is reduced, the slope of



**Figure 23.** First-cycle lift-curves for 15 cm wind tunnel model in null position at a variety of balanced cell differential pressures with crossfeed valve closed,  $30 \text{ m s}^{-1}$ .

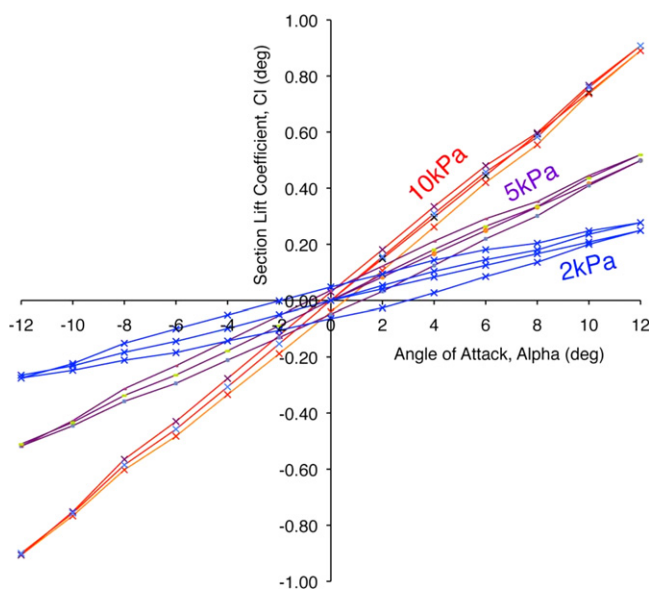


**Figure 24.** Multi-cyclic hysteretic lift-curves for 15 cm wind tunnel model in null position at a variety of balanced cell differential pressures with cross-feed valve closed,  $10 \text{ m s}^{-1}$ .

the curve degrades. It should be noted that the values shown above in 23 are simply mean lift coefficient, averaged over 1000 data points, taken at 100 Hz. The reader will note that static deformations of the airfoil induce an effective softening of the lift-curve slope such that it is approaching  $0 \text{ rad}^{-1}$  as the BCDP decreases. Although the data of figure 23 shows important trending starting from zero with a nulled airfoil configuration, it is also important to realize that as the airfoil trailing edge is allowed to freely move the data becomes highly hysteretic. Figure 24 shows the aerostructural hysteresis as a function of BCDP and angle of attack.

One of the important characteristics to note about the hysteretic behavior of the PAH airfoil is that its hysteresis is a function of the skin configuration which is manufactured to intentionally induce a level of Coulomb friction with each cycle. Such actuation friction is prescribed to make the airfoil overcritically damped so as to minimize buffet. Given shed aerodynamic structures as an artifact of wind tunnel testing, the Coulomb friction aids in reducing scatter. Another purpose of the Coulomb-damping induced hysteresis is to damp out aeromechanical modes of the entire aircraft. With that said, it is also easy to close flight control-PAH pressure manipulation loops so as to effectively eliminate hysteresis all together if desired.

## 5. FAA certifiable aircraft structures challenges: lightning strike testing

To understand how challenging it is to certify a given structure for flight on FAR 23, 25, 27 or 29 certified aircraft one needs only look at the environment and reliability levels necessary. To meet standard FAR-25.629, it is necessary for the design engineer to lay out a structure which will experience less than one catastrophic failure in 1 billion flight cycles. Typical certification temperatures include heat-soaked structures on the tarmac up to  $70^\circ\text{C}$  to high altitude flight over the tropics down to  $-80^\circ\text{C}$ . Rain and water intrusion certification are also necessary. Fatigue loads on a 1 Hz structure airframe buffet can go in excess of 100 M cycles over the lifetime of an aircraft. Additionally the structure must be resistant to lightning strike, icing and hail. As a result, aircraft structural certification is typically no easy task.

Towards this end, a lightning series of lightning strike tests were conducted on the 15 cm wind tunnel test specimen. Because many tips of flight control surfaces are in or close to lightning strike Zone 1A, B, or C, a complete strike run was conducted in the Transportation Research Institute's Lightning Strike Test Range. Two series of shots were run in succession under 58% humidity,  $22^\circ\text{C}$  at 100.6 kPa of atmospheric pressure. The first series of shots was to determine mechanical degradation in the bare metal configuration. Prior to each shot, the specimen was grounded to the grounding plate and as the Marx generator was charged to the prescribed shot level. The shot gap was set to prescribed distances so as to match the prescribed shot voltage, current and power levels. Figure 25 shows the airfoil mounted in the test range prior to and during lightning strike testing.

The shot sequences were slowly increased strike by strike, starting at just 550 kW of peak power, finally culminating at 72 MW of peak power flow at the final shot. Between each shot, the section was checked for full functionality in terms of range of motion as a function of UCDP. During shot sequence 1, it was discovered on shot #4 at 4.9 MW of peak power that the flight control surface completely seized and ceased operating. When diagnosed, it was determined that the bare metal surfaces of the sliding skins at the trailing edge had been effectively 'spot welded' together. The surfaces were then separated, cleaned and re-finished,

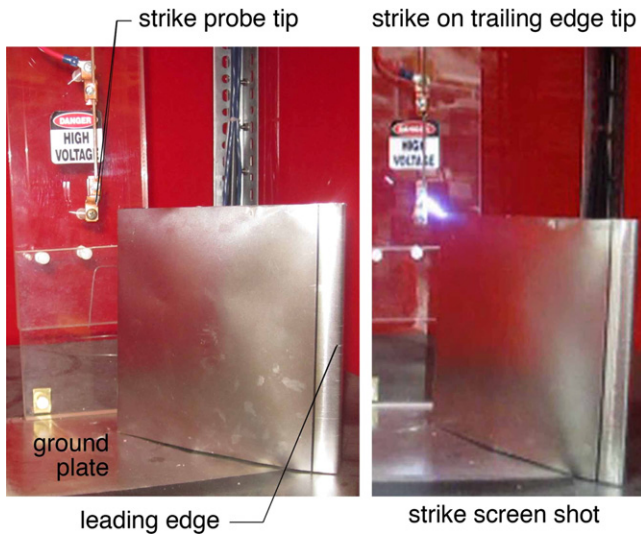


Figure 25. Setup of 15 cm wind tunnel airfoil section during lightning strike testing.

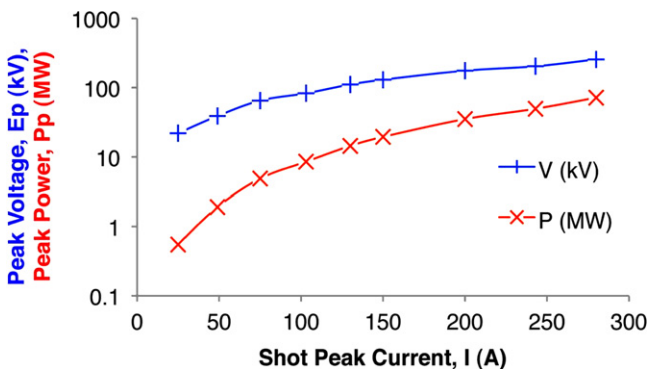


Figure 26. Lightning strike shot sequence 2 voltage and power per shot.

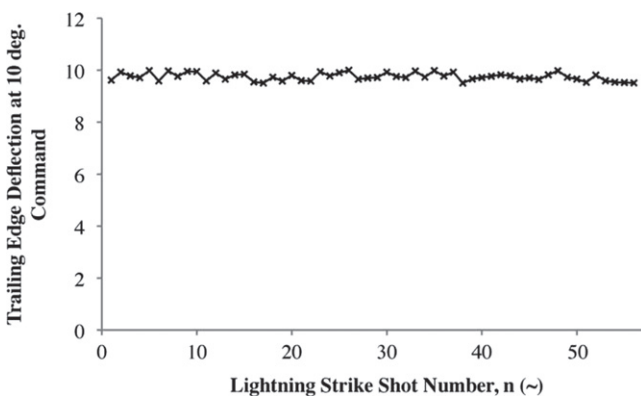


Figure 27. Effect of simulated lightning strikes on test airfoil.

then a layer of 25  $\mu\text{m}$  thick Teflon was applied to the surface for the second series of shots. From figure 26 it can be seen that the shot sequence ran all the way out to 256 kV of at 280 A of current.

Following the retrofit with Teflon coatings no further adverse characteristics in deflection manipulation following lightning strike shots were experienced. In all the airfoil was

shot a total of 56 times during the second test sequence with no failure or reduction in manipulation properties of either the honeycomb or skins. Prior to each shot, the airfoil section was commanded to a null trailing edge deflection. Following each shot, the trailing edge was commanded (open loop) to a 10° deflection level. Figure 27 shows that the deflection levels are within 0.5° of the target commanded level.

## 6. Aeromechanics modeling implications for aircraft, safety, flight characteristics, performance and operations

Some of the most important characteristics of PAH aerostuctures is that their compliance can be actively scheduled to match flight state. This stiffness matching will allow PAH-equipped lifting surfaces to function as ‘shock absorbers’ for aircraft. From figures 17 and 18, it is clear that the effective stiffness of the PAH in the most general term from an aeromechanics perspective,  $K_\delta$  can be actively manipulated by varying the BCDP. Similarly, if one considers the PAH as being integrated into a flap structure, the trailing edge angle of the flap,  $\delta_f$  can be issued a ‘command’ from a flight controller,  $\delta_{\text{command}}$  which is set by manipulating the UCDP. Such a PAH-flapped wing will have an effective rotational spring with a spring constant such that changes in angle of attack and deflection will lead to moments about an equivalent hinge point. This distributed ‘spring’ shall accordingly have a rotational stiffness of  $K_\delta$ . If one examines the moment generated about a given PAH hinge, then the aerodynamic moment can be equated to the moment generated by the rotational spring:

$$M_{\text{tot}} = c_h \bar{q} S_h \bar{c}_f = (c_{h\alpha} \alpha + c_{h\delta} \delta_f) \bar{q} S_h \bar{c}_f \quad (1)$$

$$= K_\delta (\delta_{\text{command}} - \delta_f)$$

Solving equation (1) for PAH equivalent flap deflection yields:

$$\delta_f = \frac{K_\delta \delta_{\text{command}} - c_{h\alpha} \alpha \bar{q} S_h \bar{c}_f}{K_\delta + c_{h\delta} \bar{q} S_h \bar{c}_f} \quad (2)$$

If one assumes the aircraft is flying in a range where linear relations hold for overall lift relations (typically attached flow conditions for a fundamental analysis):

$$C_L = C_{L_0} + C_{L\alpha} \alpha + C_{L\delta f} \delta_f$$

$$= C_{L_0} + C_{L\alpha} \alpha + C_{L\delta f} \left( \frac{K_\delta \delta_{\text{command}} - c_{h\alpha} \alpha \bar{q} S_h \bar{c}_f}{K_\delta + c_{h\delta} \bar{q} S_h \bar{c}_f} \right) \quad (3)$$

To make the lift coefficient insensitive to changes in angle of attack, the derivative with respect to angle of attack can be set to zero. Because a major variable that the PAH dynamically aerocompliant structures will be able to control is

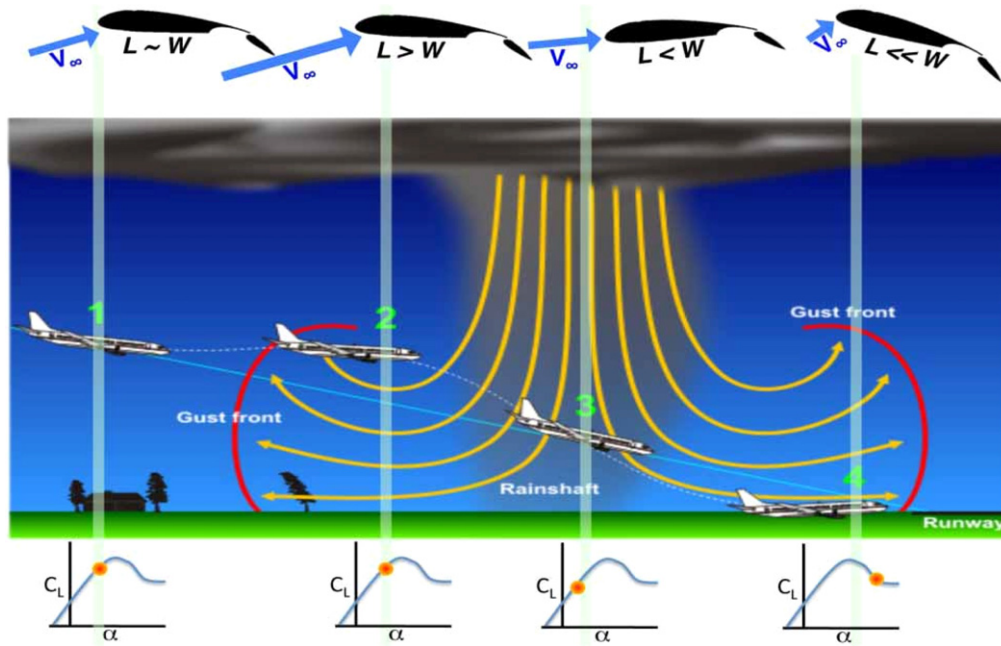


**Figure 28.** Catastrophic flight profile of aircraft with conventional flap system traversing a microburst.

the spring stiffness, that can accordingly be solved for:

$$K_{\delta} = \left( \frac{C_{L\delta_f} c_{h\alpha} - c_{h\delta}}{C_{L\alpha}} \right) \bar{q} S_h \bar{c}_f. \quad (4)$$

From equation (4), it can be seen that as the aircraft flies faster, the effective spring stiffness must be increased to maintain angle of attack insensitivity. To decouple the aircraft from dynamic pressure changes, the following relationship can be examined:

$$\begin{aligned} L &= \bar{q} S C_L = [C_{L_0} + C_{L\alpha} \alpha + C_{L\delta_f} \delta_f] \bar{q} S \\ &= \left[ C_{L_0} + C_{L\alpha} \alpha C_{L\delta_f} \right. \\ &\quad \left. \times \left( \frac{K_{\delta} \delta_{\text{command}} - c_{h\alpha} \alpha \bar{q} S_h C_f}{K_{\delta} + c_{h\delta} \bar{q} S_h C_f} \right) \right] \bar{q} S \end{aligned} \quad (5)$$

Substituting the  $K_{\delta}$  term:

$$\begin{aligned} L &= \left[ C_{L_0} + C_{L\alpha} \alpha + C_{L\delta_f} \right. \\ &\quad \left. \times \left( \frac{\left( \frac{C_{L\delta_f} c_{h\alpha} - c_{h\delta}}{C_{L\alpha}} \right) \bar{q} S_h \delta_{\text{command}} - c_{h\alpha} \alpha \bar{q} S_h}{\left( \frac{C_{L\delta_f} c_{h\alpha} - c_{h\delta}}{C_{L\alpha}} \right) \bar{q} S_h + c_{h\delta} \bar{q} S_h} \right) \right] \bar{q} S. \end{aligned} \quad (6)$$

$$L = \left[ C_{L_0} + \left( C_{L\delta_f} - C_{L\alpha} \frac{c_{h\delta}}{c_{h\alpha}} \right) \delta_{\text{command}} \right] \bar{q} S. \quad (7)$$

From equation (7), it is clear that the commanded deflection,  $\delta_{\text{command}}$  can be solved for such that the aircraft would be simultaneously insensitive to angle of attack

changes and yet produce a prescribed amount of lift:

$$\delta_{\text{command}} = \frac{\frac{L_{\text{command}}}{\bar{q} S} - C_{L_0}}{\left( C_{L\delta_f} - C_{L\alpha} \frac{c_{h\delta}}{c_{h\alpha}} \right)}. \quad (8)$$

If one considers this expression from a practical point of view, then the flight safety implications can be observed. One of the most dangerous atmospheric structures that aircraft occasionally encounter is the ‘microburst’. Figure 28 shows the structure of a typical microburst, the angle of attack and dynamic pressure variation which has led to several hundred fatalities over the past three decades including the death of 137 people in the Delta 191 crash of 1985 [33].

As the aircraft with a conventional flap system enters the windward front of the ground recirculation toroid generated by a microburst, the aircraft encounters an updraft, increase in angle of attack and increase in dynamic pressure. This in turn induces a non-trivial upward deviation from a prescribed glideslope. As the aircraft transits the midsection of the downburst, the downdraft forces the aircraft towards the ground. As the aircraft exits the leeward side of the toroid, then tailwind decreases the dynamic pressure seen by the lifting surfaces on the aircraft, resulting in a loss of lift and occasionally a catastrophic event. If one considers an adaptively aerocompliant PAH flap system, then the aeromechanics in the vicinity of a microburst are quite different as the aircraft wing would be tuned to generate a certain level of prescribed lift, with an overall stiffness set by an expression like equation (4) and a commanded deflection commanded by an expression like equation (8) rather than generating lift as a function of angle of attack (as is the case with conventional aircraft). Figure 29 shows the overall flight path of a PAH-

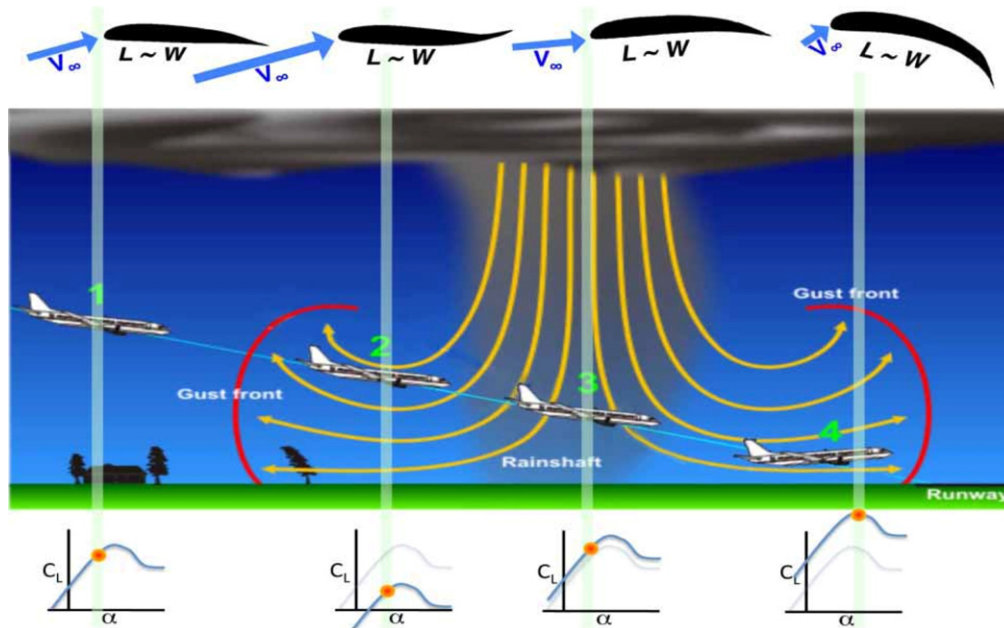


Figure 29. Safe flight profile of aircraft with PAH flap system traversing a microburst.

equipped aircraft during steady descent under microburst conditions and its steady penetration of the structure.

From figure 29 it is clear that as the PAH-equipped aircraft enters the windward side of the ground toroid, the structural compliance of the surface allows for rapid lift camber changes, thereby lowering the lift coefficient, but maintaining the same amount of total lift. The negative camber reverses as the aircraft transits the central air shaft. As the aircraft exits the leeward portion of the toroid, the section becomes highly cambered, boosting lift coefficient as the dynamic pressure and angle of attack are reduced to maintain steady lift. If one looks at the gross behavior of an aircraft as it flies through a given gust field, then it can be seen from equation (4.5) of [34] and equation (7)–(23) of [35] that the vertical acceleration of a given aircraft flying through a gust field is directly proportional to the lift curve slope of the aircraft. If a given flight director has the ability to command a reduction in lift-curve slope as shown in figure 18, then a reduction in vertical acceleration due to gusts will follow. It should be noted that dynamically aerocompliant PAH structures are not only compatible with monolithic airfoils, but can also be used on multiple-slotted airfoil sections. So although an unslotted airfoil is shown in figure 29, the reader should note that the dynamics apply to many configurations of airfoils and high lift devices. In addition to reducing gust response, it can be seen that the dynamics are fundamentally stabilizing and will help tremendously in increasing flight safety, ride quality and fatigue resistance.

## 7. Conclusions

It can be concluded that by following the basic structural models of microscopic pulvinar flexor cells in plants like *A.*

*Julibrissin*, their macroscopic equivalents, manifested in PAH can be integrated into engineered actuators which can function as artificial muscle tissues. These equivalents of artificial tissues can be built entirely from materials which are commonly found on FAR-23 and FAR-25 certified aircraft. Because all components within the actuators typically operate in the infinite-life fatigue zone, such actuators are suitable candidates for use in certified aircraft.

In addition to being fundamentally FAR-23/25 certifiable, PAH actuators are shown to possess an order of magnitude lower volumetric energy density than conventional actuators; however, PAH actuators conversely have mass-normalized energy densities which are an order of magnitude greater than conventional actuators used on FAR-23/25 certified aircraft.

Wind tunnel experimentation on a 15 cm NACA 0012 airfoil section showed that the slope of the section could be adjusted continuously from 1.2 to 6.2  $\text{rad}^{-1}$  by altering the BCDP within the section. Fully cyclical testing showed the presence of 13–42% Coulomb-friction generated hysteresis. A full run of lightning strike tests conducted to 72 MW of peak pulse power showed no degradation in deflection levels or functionality when fitted with a 25  $\mu\text{m}$  thick Teflon slip layer on sliding metal surfaces.

Basic aircraft aeromechanics modeling demonstrated that a PAH adaptive aerocompliant airfoil-equipped aircraft which possesses the ability to adjust both flap stiffness and basic camber levels can fly a ‘commanded-lift’ flight profile. Such a flight profile is accordingly shown to have the potential of increasing flight safety, fatigue life and ride quality via scheduled adjustments in overall flap system stiffness and commanded deflection levels with dynamic pressure.

## Acknowledgements

The authors wish to acknowledge the support of the US Department of Transportation under Assistance Number: DTD 559-06-G-0047 to the University of Kansas Transportation Research Institute, TRI.

## References

- [1] Crawley E F and De Luis J 1987 Use of piezoelectric actuators as elements of intelligent structures *AIAA J.* **25** 987–97
- [2] Barrett R 1992 Active plate and missile wing development using EDAP elements *Smart Mater. Struct.* **1** 214–26
- [3] Barrett R 1994 Active plate and missile wing development using directionally attached piezoelectric elements *AIAA J.* **32** 601–9
- [4] Barrett R and Brozowski F 1996 Missile flight control using active Flexspar actuators *Smart Mater. Struct.* **5** 121–8
- [5] Barrett R 1995 Method and apparatus for sensing and actuating in a desired direction *US Utility Patent No.* 5440 193 (issued 8 August)
- [6] Barrett R 2004 Adaptive aerostructures—the first decade of flight on uninhabited aerospace systems *Proc. Soc. Photo-Optical Instrumentation Engineers 11th Annual Int. Symp. on Smart Structures and Materials (San Diego, CA, March)* paper 5388-19
- [7] Barrett R, Frye P and Schliesman M 1998 Design, construction and characterization of a flightworthy piezoelectric solid state adaptive rotor *Smart Mater. Struct.* **7** 422–31
- [8] Straub F K and Merkley D J 1995 Design of a smart material actuator for rotor control *Proc. SPIE* **2443** 89–104
- [9] Straub F K and King R J 1996 Application of smart materials to control of a helicopter rotor *Proc. SPIE* **2721** 66
- [10] Straub F K, Ealey M A and Schetky L M 1997 Application of smart materials to helicopter rotor active control *Proc. SPIE* **3044** 99
- [11] Straub F K 1999 Development of a full scale smart rotor system *Proc. 8th ARO Workshop on Aeroelasticity of Rotorcraft Systems (State College, PA)*
- [12] Lesieutre G A and Davis C L 1997 Can a coupling coefficient of a piezoelectric actuator be higher than those of its active material? *J. Intell. Mater. Syst. Struct.* **8** 859–67
- [13] Lesieutre G A and Davis C L 2001 Transfer having a coupling coefficient higher than its active material *US Patent* 6236 143
- [14] Vos R, De Breuker R, Barrett R and Tiso P 2007 Morphing wing flight control via postbuckled precompressed piezoelectric actuators *J. Aircr.* **44** 1060–8
- [15] Barrett R 2008 Post-buckled precompressed (PBP) subsonic micro flight control actuators *Smart Mater. Struct.* **17** 10
- [16] Vos R and Barrett R 2010 Post-buckled precompressed techniques in adaptive aerostructures: an overview *J. Mech. Des.* **132** 031004
- [17] Barrett R 2011 (Post-buckled precompressed) Actuator *US Patent* 7898 153
- [18] Anon A 1966 *Mooney Positive Control System (M20 Series)* (Torrence, CA: Brittain Industries Division of Narco Scientific Industries)
- [19] Hanes A L 1968 *Constant Co-Pilot Model BSA-4 Pressure System* (Torrence, CA: Brittain Industries Division of Narco Scientific Industries)
- [20] Woods B K S, Bubert E A, Kothera C S and Wereley N M 2008 Design and testing of a biologically inspired pneumatic trailing edge flap system *Proc. 49th AIAA/ASME/ASCE/AHS/ASC Structures, Structural Dynamics and Materials Conf. (Schaumburg, IL)* pp 7–10
- [21] Woods B S, Kothera C S and Wereley N M 2011 Wind tunnel testing of a helicopter rotor trailing edge flap actuated via pneumatic artificial muscles *J. Intell. Mater. Syst. Struct.* **22** 1513–28
- [22] Vos R and Barrett R 2011 Mechanics of pressure adaptive honeycomb and its application to wing morphing *Smart Mater. Struct.* **20** 094010
- [23] Vos R 2009 Mechanics and applications of pressure adaptive honeycomb *PhD Dissertation* Aerospace Engineering Department, University of Kansas
- [24] Barrett R and Vos R 2013 Method and apparatus for pressure adaptive morphing structure *European Patent* EP 2459442 A2 issued June 2012, also US Patent 8366 057 B2 issued 5 February 2013
- [25] Barton L and Northrop D 2011 Cell movement and chemotaxis *Microbial Ecology* (Hoboken, NJ: Wiley) pp 68–71
- [26] Brooker J, Widmaier E, Graham L and Stiling P 2011 Skeletal muscle structure and the mechanism of force generation *Biology* 2nd edn (New York: McGraw-Hill) pp 921–8
- [27] Wilkins M 1988 Sensitive and nervous plants *Plantwatching: How Plants Remember, Tell Time, Form Relationships, and More* (New York: Facts on File) chapter 13, pp 136–42
- [28] Allen R D 1969 Mechanism of the seismonastic reaction in *Mimosa pudica Plant Physiol.* **44** 1101–7
- [29] Kanzawa N, Hoshino Y, Chiba M, Hoshino D, Kobayashi H, Kamasawa N *et al* 2006 Change in the actin cytoskeleton during seismonastic movement of *Mimosa pudica Plant Cell Physiol.* **47** 531–9
- [30] Pagitz M, Lamacchia E and Hol J M A M 2012 Pressure-actuated cellular structures *Bioinspir. Biomim.* **7** 016007
- [31] Pagitz M and Coosemans J 2012 Pressure actuated cellular structures *Leonardo Times* (Delft: Technical University of Delft) pp 38–9
- [32] Barlow J, Rae W H and Pope A 1999 *Low Speed Wind Tunnel Testing* (Hoboken, NJ: Wiley)
- [33] Smith M 2010 *From 'Adverse Winds' to Microbursts* (College Station, TX: Greenleaf Book Group Press)
- [34] Roskam J 1991 *Airplane Design, Part VII Determination of Stability, Control and Performance Characteristics: FAR and Military Requirements* (Lawrence, KS: DAR Corporation)
- [35] Torenbeek E 1982 *Synthesis of Subsonic Aircraft Design* (Delft: Delft University Press)